J. Fluid Mech. (2002), *vol.* 451, *pp.* 261–282.
DOI: 10.1017/S0022112001006516 Printed in the United Kingdom

Density-driven instabilities of miscible fluids in a Hele-Shaw cell: linear stability analysis of the three-dimensional Stokes equations

By F. GRAF[1], E. MEIBURG[1,2]† AND C. HÄRTEL[2]

[1]Department of Mechanical and Environmental Engineering, University of California, Santa Barbara, CA 93106, USA

[2]Institute of Fluid Dynamics, ETH Zürich, CH-8092 Zürich, Switzerland

(Received 7 March 2001 and in revised form 23 July)

We consider the situation of a heavier fluid placed above a lighter one in a vertically arranged Hele-Shaw cell. The two fluids are miscible in all proportions. For this configuration, experiments and nonlinear simulations recently reported by Fernandez *et al.* (2002) indicate the existence of a low-Rayleigh-number (*Ra*) 'Hele-Shaw' instability mode, along with a high-*Ra* 'gap' mode whose dominant wavelength is on the order of five times the gap width. These findings are in disagreement with linear stability results based on the gap-averaged Hele-Shaw approach, which predict much smaller wavelengths. Similar observations have been made for immiscible flows as well (Maxworthy 1989).

In order to resolve the above discrepancy, we perform a linear stability analysis based on the full three-dimensional Stokes equations. A generalized eigenvalue problem is formulated, whose numerical solution yields both the growth rate and the two-dimensional eigenfunctions in the cross-gap plane as functions of the spanwise wavenumber, an 'interface' thickness parameter, and *Ra*. For large *Ra*, the dispersion relations confirm that the optimally amplified wavelength is about five times the gap width, with the exact value depending on the interface thickness. The corresponding growth rate is in very good agreement with the experimental data as well. The eigenfunctions indicate that the predominant fluid motion occurs within the plane of the Hele-Shaw cell. However, for large *Ra* purely two-dimensional modes are also amplified, for which there is no motion in the spanwise direction. Scaling laws are provided for the dependence of the maximum growth rate, the corresponding wavenumber, and the cutoff wavenumber on *Ra* and the interface thickness. Furthermore, the present results are compared both with experimental data, as well as with linear stability results obtained from the Hele-Shaw equations and a modified Brinkman equation.

1. Introduction

The investigation of variable-density miscible flows in vertical Hele-Shaw cells has a long history. Among the first researchers to address this class of flows is Wooding (1960), who analyses situations characterized by a constant density gradient. Based on a set of approximate equations, he calculates the conditions for neutral stability in terms of a critical Rayleigh number *Ra*, where the perturbations are assumed to be of wavy form both in the horizontal and the vertical direction. He furthermore provides

† Author to whom correspondence should be addressed.

a discussion of the range of validity of the Poiseuille flow assumption. In a related experimental work several years later (Wooding 1969), the same author focuses on the unstable dynamics of a miscible interface in a Hele-Shaw cell. He observes the early stages to be dominated by diffusive growth. During the later stages the amplitudes of the evolving fingers exhibit linear growth, while their wavelength increases with time.

In a companion paper, Fernandez *et al.* (2002, henceforth referred to as FKPM), revisit gravitationally unstable, miscible flows in a vertically arranged Hele-Shaw cell. From their experiments on the early, linear phase of the instability growth, they are able to obtain information regarding the wavelength of the dominant perturbation, along with the corresponding growth rate, as a function of Ra. These data indicate the existence of a low-Ra regime in which the wavelength is inversely proportional to Ra, and a high-Ra regime with a dominant wavelength of about five times the gap width of the Hele-Shaw cell. Accompanying nonlinear numerical simulations based on the three-dimensional Stokes equations confirm the existence of qualitative differences between the low- and high-Ra regimes. In the low-Ra regime, convective transport occurs primarily in the plane of the Hele-Shaw cell. Consequently, for this so-called 'Hele-Shaw' mode the interfacial region deforms predominantly in the spanwise direction, whereas gradients in the cross-gap direction remain small. Conversely, at high Ra a 'gap' mode is seen to dominate, in which layers of the resident fluid are deposited on the walls of the cell, while fingers of the lighter fluid propagate along the central regions of the cell, cf. also Petitjeans & Maxworthy (1996), Chen & Meiburg (1996), Lajeunesse *et al.* (1997, 1999), Petitjeans *et al.* (1999). This behaviour leads to the formation of large gradients in the cross-gap direction, which immediately raises the question as to whether it can be captured by a gap-averaged Hele-Shaw approach, cf. Homsy (1987). Such gap-averaged approximate equations have been employed by several authors in order to investigate Hele-Shaw and porous media flows, both for the purpose of linear stability analyses (e.g. Tan & Homsy 1986; Yortsos 1990; Rogerson & Meiburg 1993*a*; Manickam & Homsy 1995; Wooding, Tyler & White 1997), and for fully nonlinear simulations, as reported by e.g. Tan & Homsy (1988), Manickam & Homsy (1993), Rogerson & Meiburg (1993*b*), Chen & Meiburg (1998), Ruith & Meiburg (2000). Very recently, Martin, Rakotomalala & Salin (2001) address the relationship between the stability problems for the confined gap and unbounded geometries, cf. also the earlier work by Taylor (1950), Chandrasekhar (1961), and Batchelor & Nitsche (1991) for an unbounded stratified fluid, and by Batchelor & Nitsche (1993) for stratified fluid contained in a vertical cylinder.

The above observations for miscible flows have corresponding counterparts for immiscible two-phase flows in Hele-Shaw cells. In viscously driven flows, at low capillary numbers Ca the curved interface front extends across the entire gap, cf. Park & Homsy (1985), whereas at large Ca a wetting layer is left behind on the walls of the cell (Bretherton 1961; Park & Homsy 1984; Schwartz 1986). Experimental measurements by Park, Gorell & Homsy (1984) and Maxworthy (1989) show that the predictions for the dominant wavelength obtained from the Hele-Shaw equations by Chuoke, Van Meurs & Van der Poel (1959) as well as Saffman & Taylor (1958) are accurate only in the limit of small Ca. For larger Ca values, the dominant wavelength is again seen to scale with the gap width of the Hele-Shaw apparatus.

The present investigation addresses the reasons for the disagreement between experimental observations and predictions by the Hele-Shaw equations regarding such quantities as the dominant wavelengths and the corresponding growth rates. For viscously driven flows, a first step in this direction was taken by Paterson (1985). Using the criterion that the flow will tend to a state of minimal dissipation, he showed that

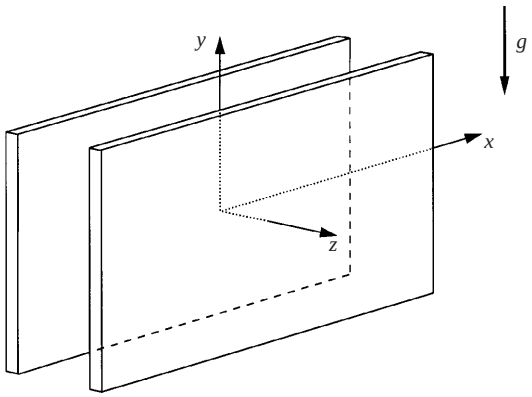

FIGURE 1. Hele-Shaw cell with coordinate system.

the wavelength of maximum growth in the absence of diffusion and surface tension is approximately four times the gap width, provided that the less viscous fluid is essentially inviscid. However, this argument cannot be extended to constant-viscosity, variable-density situations such as the one of interest here. Consequently, we approach the task of determining the most amplified wavelength, along with the corresponding growth rate, by means of a linear stability analysis of the full three-dimensional Stokes equations in a vertical Hele-Shaw cell. In this way, the effects of cross-gap velocities and concentration gradients can be included in the analysis, which is not possible with the gap-averaged Hele-Shaw approach.

The paper is structured as follows: The physical problem, along with the governing equations and their non-dimensionalization, is described in more detail in § 2. These equations are linearized, and the numerical procedure for the solution of the resulting eigenvalue problem is discussed. Both two-dimensional, i.e. cross-gap, and three-dimensional perturbations are considered. In § 3 the results of the stability analysis regarding the dominant wavenumber and its growth rate are presented. Furthermore, the commonly employed 'extended Hele-Shaw' equations, or Darcy's law, are analysed in some detail, and the validity of the underlying assumptions is discussed. Stability predictions obtained from these Hele-Shaw equations are compared with the present results for the Stokes equations. In addition, comparisons with the experimental data of FKPM and the modified Brinkman equation approach of those authors are presented. Section 4 states the main conclusions to be drawn from the stability results.

2. Physical problem

2.1. *Governing equations*

We consider the situation of a heavier fluid placed above a lighter one in a vertically arranged Hele-Shaw cell with a gap width e, cf. figure 1. The two fluids are miscible in all proportions, and we assume that their motion is governed by the three-dimensional Stokes equations

$$\nabla \cdot \boldsymbol{u} = 0, \tag{2.1}$$

$$\nabla p = \mu \nabla^2 \boldsymbol{u} - \rho \boldsymbol{g}, \tag{2.2}$$

$$\frac{\partial c}{\partial t} + \boldsymbol{u} \cdot \nabla c = D \nabla^2 c. \tag{2.3}$$

It should be pointed out that the convective term in the concentration equation renders the above set of equations nonlinear; $\boldsymbol{u}$ represents the flow velocity, $\boldsymbol{g}$ denotes the vector of gravitational acceleration, which is taken to point in the $-y$-direction, and c indicates the concentration of the heavier fluid. Note that implicitly contained in the above set of conservation equations is the Boussinesq approximation, which assumes that the solute concentration affects the local density without causing an expansion or contraction of the fluid. Both the viscosity μ and the diffusion coefficient D are considered constant throughout the mixture. The density ρ is assumed to vary linearly with c according to

$$\rho = \rho_2 + c(\rho_1 - \rho_2), \tag{2.4}$$

where ρ_1 and ρ_2 represent the densities of the heavier and lighter fluid, respectively. To render the governing equations dimensionless, we introduce a characteristic length L^*, velocity U^*, time T^*, pressure P^* and density difference R^* in the form of

$$L^* = e, \tag{2.5}$$

$$U^* = \frac{\Delta\rho\, g\, e^2}{\mu}, \tag{2.6}$$

$$T^* = \frac{\mu}{\Delta\rho\, g\, e}, \tag{2.7}$$

$$P^* = \Delta\rho\, g\, e, \tag{2.8}$$

$$R^* = \Delta\rho = \rho_1 - \rho_2, \tag{2.9}$$

cf. also FKPM. In this way, we obtain the dimensionless set of equations

$$\nabla \cdot \boldsymbol{u} = 0, \tag{2.10}$$

$$\nabla p = \nabla^2 \boldsymbol{u} - c\nabla y, \tag{2.11}$$

$$\frac{\partial c}{\partial t} + \boldsymbol{u} \cdot \nabla c = \frac{1}{Ra}\nabla^2 c, \tag{2.12}$$

where the Rayleigh number is defined as

$$Ra = \frac{\Delta\rho\, g\, e^3}{D\mu}. \tag{2.13}$$

2.2. *Linearization and formulation of the eigenvalue problem*

We linearize the above system of equations around a quiescent base state

$$\begin{pmatrix} u \\ v \\ w \\ p \\ c \end{pmatrix}(x, y, z, t) = \begin{pmatrix} 0 \\ 0 \\ 0 \\ \bar{p} \\ \bar{c} \end{pmatrix}(y) + \begin{pmatrix} u' \\ v' \\ w' \\ p' \\ c' \end{pmatrix}(x, y, z, t) \tag{2.14}$$

characterized by the concentration profile

$$\bar{c} = 0.5 + 0.5\,\mathrm{erf}\left(\frac{y}{\delta}\right), \tag{2.15}$$

where the parameter δ characterizes the thickness of the interfacial region. In the following, we assume that the diffusive time scale of the base state is much larger than the characteristic time scale of the instability growth, so that δ can be held constant

for the purpose of evaluating the instability growth rate. The perturbations, denoted by a prime, are assumed to be of the form

$$\begin{pmatrix} u' \\ v' \\ w' \\ p' \\ c' \end{pmatrix}(x,y,z,t) = \begin{pmatrix} \hat{u}(y,z)\,\sin(\beta x) \\ \hat{v}(y,z)\,\cos(\beta x) \\ \hat{w}(y,z)\,\cos(\beta x) \\ \hat{p}(y,z)\,\cos(\beta x) \\ \hat{c}(y,z)\,\cos(\beta x) \end{pmatrix} \mathrm{e}^{\sigma t}, \tag{2.16}$$

where the hatted quantities represent the two-dimensional eigenfunctions. By substituting the above into the dimensionless conservation equations, subtracting out the base state, and linearizing, we obtain the system of linear equations

$$\beta\hat{u}(y,z) + \frac{\partial}{\partial y}\hat{v}(y,z) + \frac{\partial}{\partial z}\hat{w}(y,z) = 0, \tag{2.17}$$

$$\beta\hat{p}(y,z) = \beta^2\hat{u}(y,z) - \frac{\partial^2\hat{u}}{\partial y^2} - \frac{\partial^2\hat{u}}{\partial z^2}, \tag{2.18}$$

$$\frac{\partial}{\partial y}\hat{p}(y,z) = -\beta^2\hat{v}(y,z) + \frac{\partial^2\hat{v}}{\partial y^2} + \frac{\partial^2\hat{v}}{\partial z^2} - \hat{c}(y,z), \tag{2.19}$$

$$\frac{\partial}{\partial z}\hat{p}(y,z) = -\beta^2\hat{w}(y,z) + \frac{\partial^2\hat{w}}{\partial y^2} + \frac{\partial^2\hat{w}}{\partial z^2}, \tag{2.20}$$

$$\sigma\hat{c}(y,z) + \frac{\partial\bar{c}}{\partial y}\hat{v} = \frac{1}{Ra}\left(-\beta^2\hat{c}(y,z) + \frac{\partial^2\hat{c}}{\partial y^2} + \frac{\partial^2\hat{c}}{\partial z^2}\right). \tag{2.21}$$

2.3. *Numerical implementation*

The above system of linearized equations is discretized on a domain that extends from wall to wall, i.e. from -0.5 to 0.5, in the cross-gap z-direction, and from $-l/2$ to $l/2$ in the vertical y-direction. Here l has to be chosen sufficiently large so that its effect on the numerical results for the eigenvalue and eigenfunctions is negligible. Test calculations show that as long as the computational domain extends at least one perturbation wavelength above and below the interface, i.e. as long as

$$l = \frac{4\pi}{\beta}, \tag{2.22}$$

the error in the magnitude of σ is below 0.1%, Consequently, this value of l is adopted for most of the calculations to be discussed below. However, for large wavenumbers a minimum value of $l = 4$ is always maintained, in order not to truncate the computational domain too close to the interfacial region.

In the z-direction, the linear equations (2.17)–(2.21) are discretized by compact finite differences (Lele 1992) of fourth order at the walls, and up to tenth order in the interior of the domain. In the y-direction, a Chebyshev collocation method is employed with two separate subdomains that cover the regions $y \geqslant 0$ and $y \leqslant 0$, respectively. This allows us to concentrate the numerical resolution in the interfacial region. At the element boundaries, the variables and their first derivatives are continuous. The vertical domain boundaries are sufficiently far away from the interface that for all velocity components and the concentration perturbation, homogeneous Dirichlet conditions can be prescribed. At the solid walls, all velocity components are assumed to vanish, along with the normal derivative of the concentration perturbation. No

boundary conditions need to be prescribed for the pressure. The required numerical resolution is established by means of test calculations. These indicate that for most cases $N_z = 17$ points in the cross-gap direction are sufficient to keep the error in the eigenvalue below 0.1%. The required number of grid points N_y in the vertical direction depends on both the interface thickness parameter δ, and the size of the computational domain, which in turn is a function of the wavenumber β. The largest calculations employ up to $N_y = 77$ and $N_z = 29$ points, which results in a matrix of size $5N_yN_z \times 5N_yN_z = 11\,165 \times 11\,165$.

Upon discretization, the system of linear equations (2.17)–(2.21) can be written in matrix form as

$$\boldsymbol{A}\boldsymbol{\phi} = \sigma\, \boldsymbol{B}\boldsymbol{\phi}. \tag{2.23}$$

Here the matrices $\boldsymbol{A}$ and $\boldsymbol{B}$ and the eigenvector $\boldsymbol{\phi}$ are of the following form

$$\begin{pmatrix} \mathbf{0} & \beta\boldsymbol{I} & \dfrac{\partial}{\partial y} & \dfrac{\partial}{\partial z} & \mathbf{0} \\ \beta\boldsymbol{I} & \boldsymbol{M}_1 & \mathbf{0} & \mathbf{0} & \mathbf{0} \\ -\dfrac{\partial}{\partial y} & \mathbf{0} & \boldsymbol{M}_1 & \mathbf{0} & -\boldsymbol{I} \\ -\dfrac{\partial}{\partial z} & \mathbf{0} & \mathbf{0} & \boldsymbol{M}_1 & \mathbf{0} \\ \mathbf{0} & \mathbf{0} & -\dfrac{\partial \bar{c}}{\partial y} & -\dfrac{\partial \bar{c}}{\partial z} & \boldsymbol{M}_2 \end{pmatrix} \begin{pmatrix} \hat{p} \\ \hat{u} \\ \hat{v} \\ \hat{w} \\ \hat{c} \end{pmatrix} = \sigma \begin{pmatrix} \mathbf{0} & \mathbf{0} & \mathbf{0} & \mathbf{0} & \mathbf{0} \\ \mathbf{0} & \mathbf{0} & \mathbf{0} & \mathbf{0} & \mathbf{0} \\ \mathbf{0} & \mathbf{0} & \mathbf{0} & \mathbf{0} & \mathbf{0} \\ \mathbf{0} & \mathbf{0} & \mathbf{0} & \mathbf{0} & \mathbf{0} \\ \mathbf{0} & \mathbf{0} & \mathbf{0} & \mathbf{0} & \boldsymbol{I} \end{pmatrix} \begin{pmatrix} \hat{p} \\ \hat{u} \\ \hat{v} \\ \hat{w} \\ \hat{c} \end{pmatrix} \tag{2.24}$$

with

$$\boldsymbol{M}_1 = -\beta^2 \boldsymbol{I} + \frac{\partial^2}{\partial y^2} + \frac{\partial^2}{\partial z^2}, \tag{2.25}$$

$$\boldsymbol{M}_2 = \frac{1}{Ra}\left(-\beta^2 \boldsymbol{I} + \frac{\partial^2}{\partial y^2} + \frac{\partial^2}{\partial z^2}\right). \tag{2.26}$$

This system has to be solved numerically in order to determine the eigenvalue σ along with the corresponding eigenfunctions $\hat{u}$, $\hat{v}$, $\hat{w}$, $\hat{p}$, and $\hat{c}$ as functions of the spanwise wavenumber β for the two parameters characterizing the overall fluid system and the base state, Ra and δ.

The numerical eigenvalue problem is solved iteratively for the leading eigenvalues by an Arnoldi method (Sorensen 1992). For the computational implementation we make use of the public domain software package ARPACK (Maschhoff & Sorensen 1996; Lehoucq, Sorensen & Yang 1998). Test calculations demonstrate that in this way the eigenvalues can be computed to a high degree of accuracy. However, the corresponding eigenfunctions are not always fully converged, and the overall rate of convergence is quite slow at times. The root of this problem can be traced back to the fact that matrix $\boldsymbol{B}$ contains very few non-zero elements on the diagonal. In order to accelerate the convergence, and to improve the accuracy, we consequently modify the original system of equations slightly to

$$\nabla \cdot \boldsymbol{u} = 0, \tag{2.27}$$

$$Re\,\frac{\partial \boldsymbol{u}}{\partial t} + \nabla p = \nabla^2 \boldsymbol{u} - c\nabla y, \tag{2.28}$$

$$\frac{\partial c}{\partial t} + \boldsymbol{u} \cdot \nabla c = \frac{1}{Ra}\nabla^2 c, \tag{2.29}$$

Re	Computed eigenvalue	Residual ξ
0	1.23061×10^{-2}	2.51376
0.001	1.23061×10^{-2}	3.55297×10^{-9}
0.01	1.23061×10^{-2}	3.31699×10^{-12}
0.1	1.23057×10^{-2}	3.19916×10^{-12}
1	1.22919×10^{-2}	9.78586×10^{-13}

TABLE 1. Eigenvalues and eigenfunction residuals for $\delta = 1$, $Ra = 10^5$, $\beta = 5$, and various values of *Re*.

where *Re* represents an artificial, Reynolds-number-like parameter. Test results shown in table 1 for $\delta = 1$, $Ra = 10^5$, $\beta = 5$, and various values of *Re*, demonstrate that for $Re = 0.01$ the magnitude of the eigenvalue is essentially unaffected by *Re*, whereas the eigenfunctions are much better converged than for $Re = 0$. Consequently, this value of *Re* is employed throughout the present investigation.

2.4. *Two-dimensional perturbations*

When studying the stability behaviour for small spanwise wavenumbers β, condition (2.22) demonstrates the need for large computational domains. The simultaneous requirement to maintain a sufficiently fine resolution of the narrow interfacial region results in exceedingly large matrix sizes, so that β cannot be made arbitrarily small. Furthermore, it is not clear that three-dimensional modes for $\beta \to 0$ will asymptote towards the two-dimensional case $\beta = 0$. For this reason, and in order to obtain information on the stability of purely two-dimensional perturbations, we consider the case of $\beta = 0$ separately, i.e. of perturbations across the gap in the absence of spanwise variations. Under these conditions, the spanwise u-velocity component vanishes identically, and we can conveniently formulate the two-dimensional governing equations in terms of the streamfunction (ψ) and vorticity (ω) variables

$$\nabla^2\psi + \omega = 0, \tag{2.30}$$

$$Re\,\frac{\partial\omega}{\partial t} + \nabla^2\omega - \frac{\partial c}{\partial z} = 0, \tag{2.31}$$

$$\frac{\partial c}{\partial t} + \boldsymbol{u}\cdot\nabla c = \frac{1}{Ra}\nabla^2 c. \tag{2.32}$$

Note that we keep the artificial parameter *Re* for the same reasons as above. Vorticity and streamfunction are defined in the usual way by

$$w = \frac{\partial\psi}{\partial y}, \quad v = -\frac{\partial\psi}{\partial z} \tag{2.33}$$

and

$$\omega = \frac{\partial v}{\partial z} - \frac{\partial w}{\partial y}. \tag{2.34}$$

Upon introducing perturbations of the form

$$\begin{pmatrix} \psi' \\ \omega' \\ c' \end{pmatrix}(y,z,t) = \begin{pmatrix} \hat{\psi}(y,z) \\ \hat{\omega}(y,z) \\ \hat{c}(y,z) \end{pmatrix} \mathrm{e}^{\sigma t}, \tag{2.35}$$

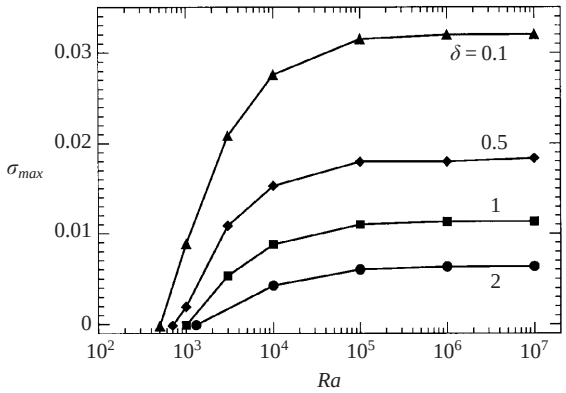

FIGURE 2. The maximum eigenvalue σ_{max} as a function of Ra, for different interface thicknesses δ.

into equations (2.30)–(2.32), linearizing, and discretizing, we obtain an eigenvalue system of the form

$$\begin{pmatrix} \boldsymbol{M}_1 & \boldsymbol{I} & \boldsymbol{0} \\ \boldsymbol{0} & \boldsymbol{M}_1 & -\dfrac{\partial}{\partial z} \\ \boldsymbol{M}_3 & \boldsymbol{0} & \boldsymbol{M}_2 \end{pmatrix} \begin{pmatrix} \hat{\psi} \\ \hat{\omega} \\ \hat{c} \end{pmatrix} = \sigma \begin{pmatrix} \boldsymbol{0} & \boldsymbol{0} & \boldsymbol{0} \\ \boldsymbol{0} & Re\boldsymbol{I} & \boldsymbol{0} \\ \boldsymbol{0} & \boldsymbol{0} & \boldsymbol{I} \end{pmatrix} \begin{pmatrix} \hat{\psi} \\ \hat{\omega} \\ \hat{c} \end{pmatrix} \tag{2.36}$$

with

$$\boldsymbol{M}_1 = \frac{\partial}{\partial y} + \frac{\partial}{\partial z}, \tag{2.37}$$

$$\boldsymbol{M}_2 = \frac{1}{Ra}\left(\frac{\partial^2}{\partial y^2} + \frac{\partial^2}{\partial z^2}\right) + \frac{\partial \bar{\psi}}{\partial z}\frac{\partial}{\partial y} - \frac{\partial \bar{\psi}}{\partial y}\frac{\partial}{\partial z}, \tag{2.38}$$

$$\boldsymbol{M}_3 = \left(\frac{\partial \bar{c}}{\partial y}\frac{\partial}{\partial z} - \frac{\partial \bar{c}}{\partial z}\frac{\partial}{\partial y}\right). \tag{2.39}$$

Along the solid walls, we specify $\hat{\psi} = 0$ and $\partial\hat{\psi}/\partial z = 0$ along with $\partial\hat{c}/\partial z = 0$. At the far-field boundaries, all perturbations are assumed to vanish.

2.5. *Validation*

As discussed above, convergence studies serve to establish the required numerical resolution, along with the necessary vertical extent of the computational domain. In addition, the computational approach is validated by comparing the growth rates with those obtained from the fully nonlinear code of FKPM for small perturbation amplitudes.

3. Results

3.1. *Two-dimensional perturbations*

We begin by discussing two-dimensional perturbations, i.e. perturbations that vary across the gap, but not in the spanwise direction. Figure 2 shows the maximum eigenvalue σ_{max} as a function of the Rayleigh number for different values of the interfacial thickness parameter δ. In general, thinner interfaces and larger Ra values are seen to be destabilizing. For each δ, a critical value Ra_{crit} can be identified, below

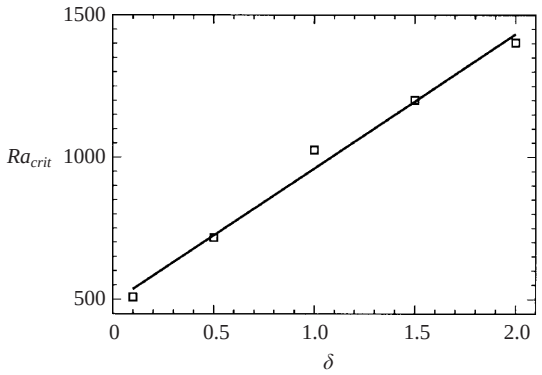

FIGURE 3. The critical Rayleigh number Ra_{crit} as a function of the interfacial thickness parameter δ, for two-dimensional perturbations. The squares represent the results of the stability calculations, and the straight line is a linear regression for these data.

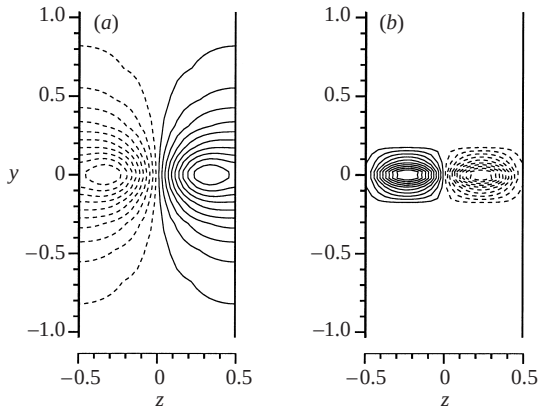

FIGURE 4. Isocontours of the concentration eigenfunctions $\hat{c}$ for $\delta = 0.1$: (*a*) the low-*Ra* mode for $Ra = 10^3$, (*b*) the high-*Ra* mode for $Ra = 10^7$. Solid (dashed) lines represent positive (negative) values. At low *Ra* values, the eigenfunction has its maximum values near the walls, whereas at large *Ra* values, the perturbation decreases to near zero at the wall.

which the base state is stable to two-dimensional perturbations. The critical *Ra*-value reflects the stabilizing influence of the walls of the cell. This observation is consistent with the nonlinear simulations discussed in FKPM. It is also in agreement with the findings of Batchelor & Nitsche (1991), as well as Batchelor & Nitsche (1993). For an unbounded stratified fluid, these authors observe all positive Rayleigh numbers to be unstable, whereas cylindrical boundaries are seen to result in a non-zero critical Rayleigh number. For large Rayleigh numbers, the present results show that the growth rate asymptotically reaches a plateau, whose value depends on δ.

Figure 3 depicts the critical Rayleigh number Ra_{crit} as a function of δ. For $0.1 \leqslant \delta \leqslant 2$, Ra_{crit} is seen to grow approximately linearly with the interface thickness. By performing a linear regression, we obtain the relationship

$$Ra_{crit} = 472.46\,\delta + 489.06. \tag{3.1}$$

This indicates that Rayleigh numbers below $O(500)$ are always stable with respect to two-dimensional perturbations. By extrapolating the maximum growth rates as a

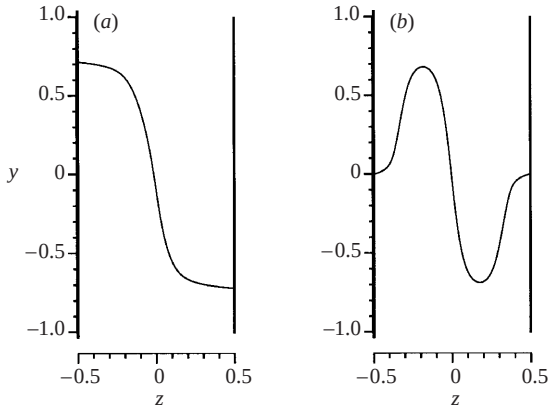

FIGURE 5. Sketch of the qualitative nonlinear concentration contours for $\delta = 0.1$ and $Ra = 10^3$ (a) and $Ra = 10^7$ (b). Compare with the nonlinear simulation results provided in FKPM.

function of δ for $Ra = 10^7$ to $\delta = 0$, we find that the maximum eigenvalue for a step-like concentration base state is approximately 0.036.

Figure 4 displays the concentration eigenfunctions for $\delta = 0.1$ and the two Ra values of 10^3 and 10^7. We can clearly distinguish a low-Ra mode, for which the concentration perturbations reach a maximum near or at the walls, and a high-Ra mode characterized by nearly vanishing perturbation levels at the wall. Since the corresponding streamfunction and vorticity eigenfunctions for these Ra values are very similar to each other, the differences in the concentration eigenfunctions are predominantly due to the effects of the diffusive term in the concentration equation.

Qualitative sketches of nonlinear interfacial shapes corresponding to the high- and low-Ra concentration eigenfunctions are given in figure 5. For low Ra values the fingers are wider and propagate up and down the solid walls, whereas for higher Rayleigh numbers we find narrower fingers growing in the central regions of the gap. It should be pointed out that for all of the parameter combinations investigated, the maximum eigenvalue never corresponded to an eigenmode with more than two fingers.

3.2. *Three-dimensional perturbations*

Figure 6 shows dispersion relationships for $\delta = 0.1$ and several Rayleigh numbers ranging from 50 to 10^7. For small and intermediate wavenumbers, the curves for $Ra > 10^5$ become indistinguishable, which indicates that a further increase in Ra affects only the range of unstable wavenumbers, i.e. the short-wavelength cutoff, but not the wavenumber of maximum growth or its growth rate.

In order to provide insight into the long-wavelength limit, figure 7 presents detailed information regarding the small-wavenumber regime, for the same parameter values as in figure 6. The data demonstrate that for each Ra value there always exists a three-dimensional perturbation that is more unstable than its two-dimensional counterpart. However, as long as the base state is unstable to two-dimensional perturbations, their growth rates are consistently higher than the values that one would obtain by extrapolating the three-dimensional curve to $\beta = 0$. This indicates that the two- and three-dimensional modes are fundamentally different in nature, which is confirmed by figure 8. In this context, it is interesting to compare with the unbounded geometry results of Batchelor & Nitsche (1991). These authors consider disturbances that are

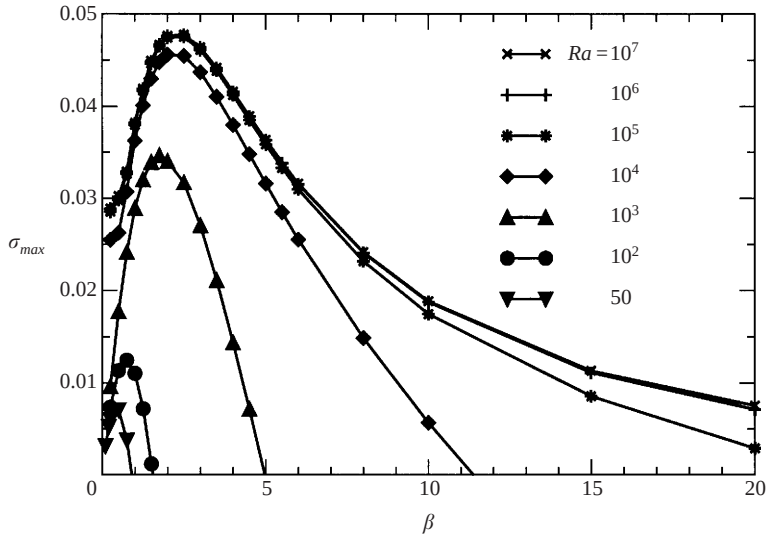

FIGURE 6. Dispersion relationships of three-dimensional perturbations for $\delta = 0.1$ and various Ra.

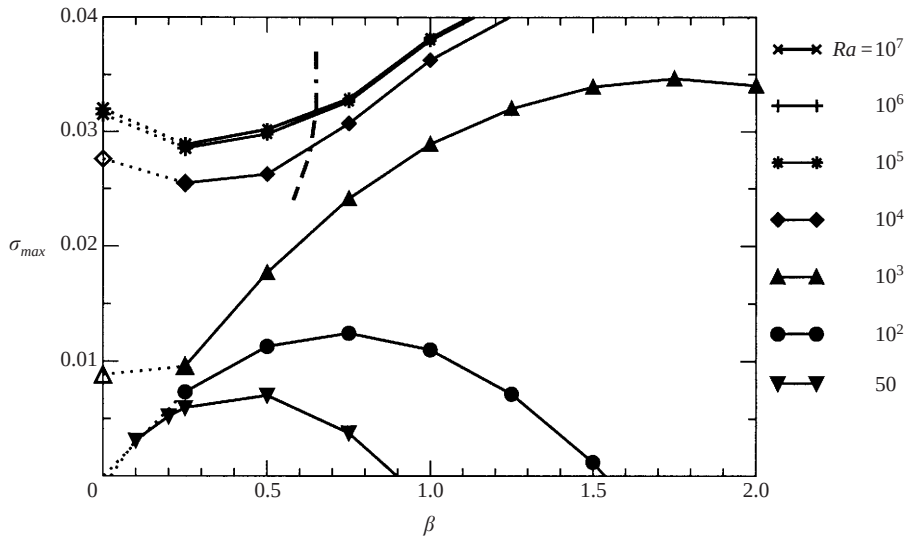

FIGURE 7. Detail of figure 6 for the small-wavenumber regime. The open symbols on the ordinate, which represent results obtained for two-dimensional perturbations, are connected by dotted lines to the solid symbols for three-dimensional disturbances. To the left of the dashed line, the unstable modes are of the shape shown in figure 10, whereas to the right of this line they resemble figure 9.

two-dimensional in nature, and they observe that the growth rate approaches zero as the wavenumber becomes smaller and smaller. In the present case, we allow for three-dimensional perturbations, and as a result variations in the cross-gap direction have the potential of triggering instabilities even as the spanwise wavenumber approaches zero.

The general shape of the eigenfunctions for the dominant three-dimensional perturbations can be seen from figure 9. The three-dimensional nature of these perturbations is clear not only from the existence of a spanwise velocity component $\hat{u}$, but also from

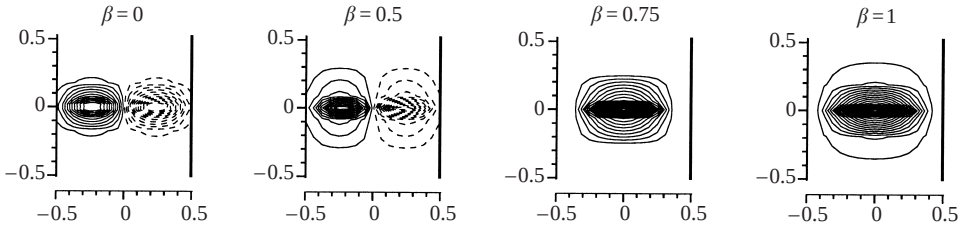

FIGURE 8. Isocontours of the concentration eigenfunction $\hat{c}$ for different wavenumbers β with $Ra = 10^5$ and $\delta = 0.1$.

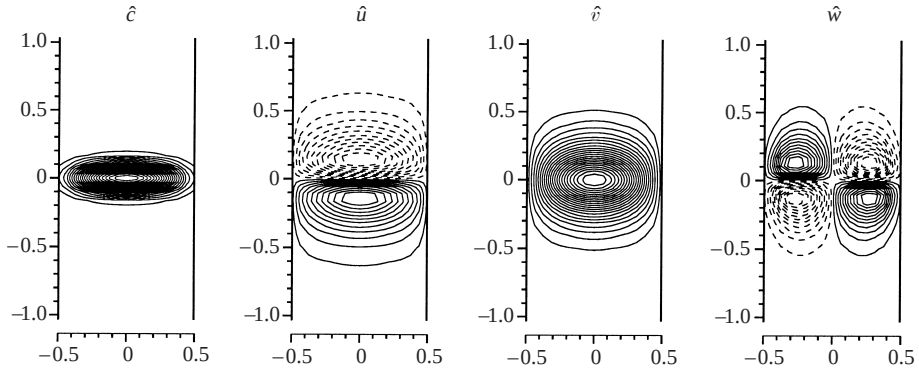

FIGURE 9. Eigenfunction contours for $Ra = 10^5$, $\delta = 0.1$, and $\beta = 10$.

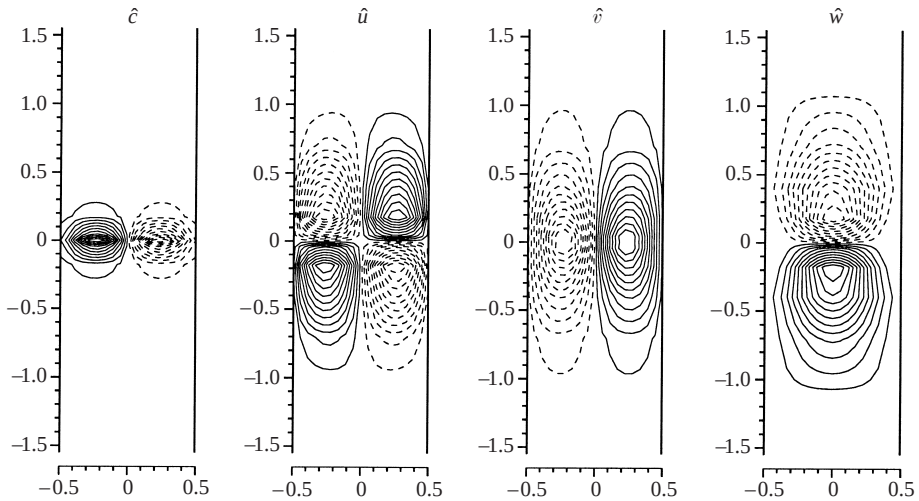

FIGURE 10. Eigenfunction contours for $Ra = 10^5$, $\delta = 0.1$, and $\beta = 0.25$.

the fact that at a given spanwise location both the concentration and the vertical velocity perturbations are of a single sign only. For long wavelengths, the eigenfunctions are of the general shape shown in figure 10.

For larger values of δ, the corresponding dispersion relationships are presented in figure 11. We observe a general trend of decreasing growth rates and smaller cutoff wavenumbers for increasing interface thicknesses.

Figure 12 displays the eigenvalue σ_{max} of the most amplified wavenumber as a

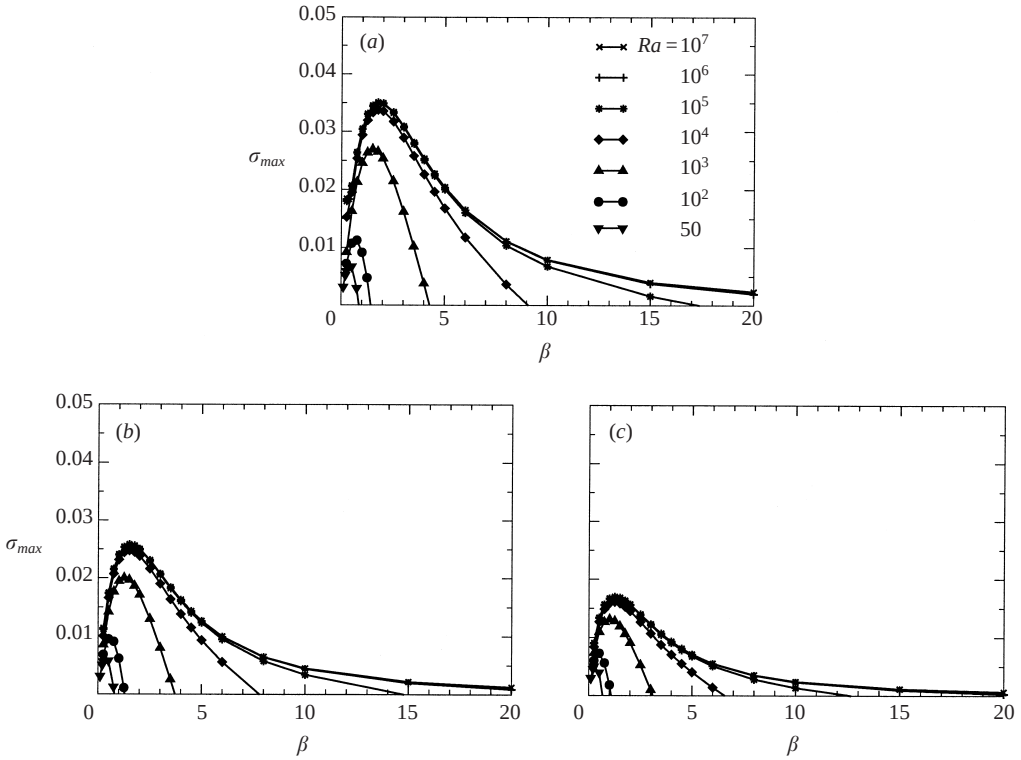

FIGURE 11. Dispersion relationships for (*a*) $\delta = 0.5$, (*b*) 1 and (*c*) 2, and for various Rayleigh numbers.

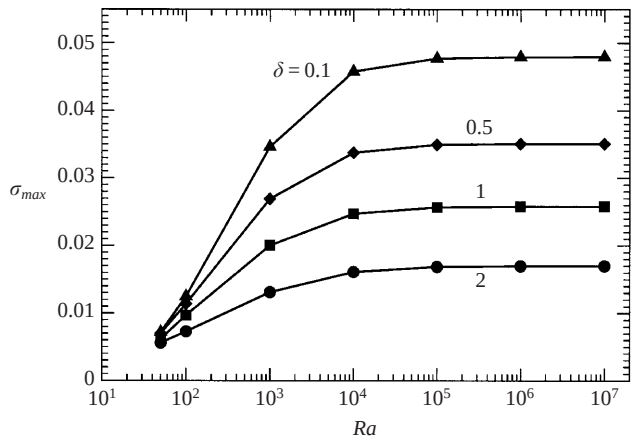

FIGURE 12. Eigenvalue σ_{max} corresponding to the most amplified wavenumber as a function of Ra for different values of δ.

function of the Rayleigh number for various interface thickness parameters. While this graph resembles figure 2 for the two-dimensional case in that it reaches a plateau for large Rayleigh numbers, the eigenvalues are generally higher, and for the same δ the unstable range extends to lower values of Ra. We did not analyse the regime $Ra < 50$, since the dominant waves become quite long, resulting in a large

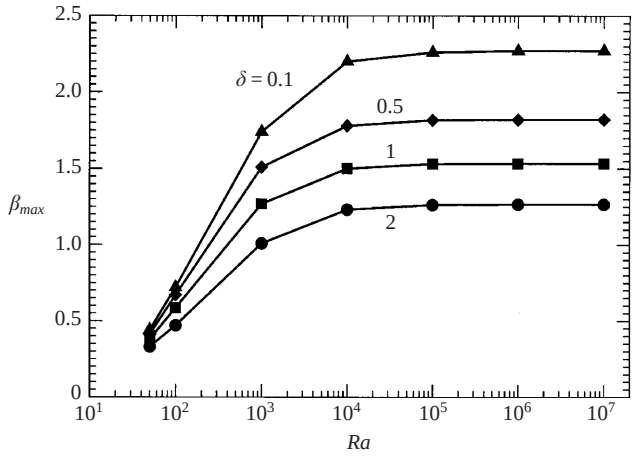

FIGURE 13. β_{max} as a function of the Rayleigh number for various interface thickness parameters δ.

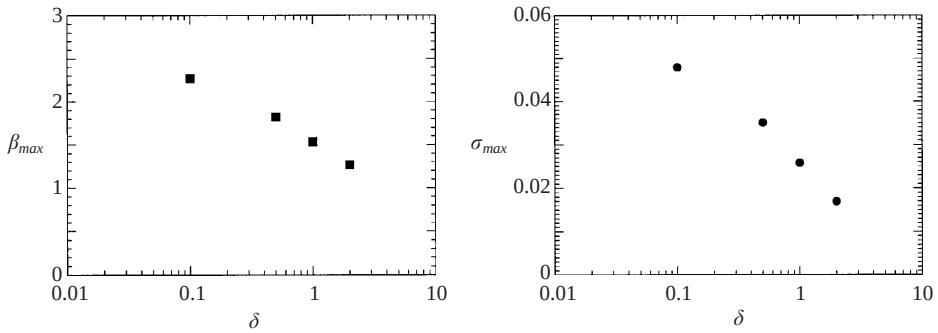

FIGURE 14. The high-Ra limit of σ_{max} along with the corresponding wavenumber β_{max} as a function of the interface thickness parameter δ.

computational domain and correspondingly expensive computations. With respect to two-dimensional perturbations, all possible base states had been stable for $Ra < 489$, whereas under three-dimensional disturbances, all δ values are still unstable for $Ra = 50$. It is interesting to see that for small Ra values the curves for different δ appear to move closer together.

The wavenumber of maximum growth β_{max} is shown in figure 13 as a function of Ra for various values of δ. It is interesting to observe that β_{max} reaches a plateau as well for large Rayleigh numbers. In general, the most amplified wavelength increases with the interfacial thickness. For a given interface thickness, it increases with decreasing Ra.

Figure 14 displays the plateau values of the maximum growth rate σ_{max} along with the corresponding wavenumber β_{max} as functions of δ in a semi-logarithmic fashion. The largest three values of δ suggest a logarithmic dependence, which, if it persists to even higher δ values, indicates that beyond a critical thickness parameter of $O(10)$ all perturbations are stable. However, we did not explicitly check for the existence of such a critical value.

The cutoff wavenumber β_{crit} is shown in figure 15 as function of the Rayleigh number for various interface thickness parameters δ. The dashed line suggests that in the limit of large Ra values, β_{crit} grows approximately in proportion to $Ra^{10/33}$.

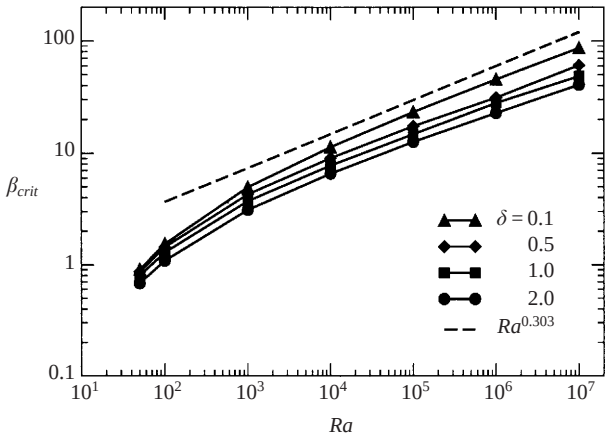

FIGURE 15. Cutoff wavenumber β_{crit} as a function of Ra for various δ. The dashed line represents the power law $\beta_{crit} \sim Ra^{10/33}$.

3.3. *Comparison with stability analysis based on the Hele-Shaw approach*

3.3.1. *Properties of the extended Hele-Shaw equations*

It is well known that for a single fluid of constant density and viscosity in a Hele-Shaw cell, the three-dimensional Stokes equations are solved exactly by

$$u(x, y, z) = \tfrac{3}{2}u_0(x, y)\left(1 - 4\frac{z^2}{e^2}\right), \tag{3.2}$$

$$v(x, y, z) = \tfrac{3}{2}v_0(x, y)\left(1 - 4\frac{z^2}{e^2}\right), \tag{3.3}$$

$$w(x, y, z) = 0, \tag{3.4}$$

$$\frac{\partial p}{\partial x} = -\frac{12\mu}{e^2}u_0(x, y), \tag{3.5}$$

$$\frac{\partial p}{\partial y} = -\frac{12\mu}{e^2}v_0(x, y), \tag{3.6}$$

provided that the gap-averaged velocities u_0 and v_0 in the plane of the Hele-Shaw cell satisfy the equations of two-dimensional, incompressible irrotational flow. Several authors have extended this approach and analysed Stokes flows involving two miscible fluids of different densities, which are governed by the set of equations (2.1)–(2.3), on the basis of a set of 'augmented' Hele-Shaw equations, which are also referred to as the Darcy equations

$$\frac{\partial u_0}{\partial x} + \frac{\partial v_0}{\partial y} = 0, \tag{3.7}$$

$$\frac{\partial p}{\partial x} = -\frac{12\mu}{e^2}u_0, \tag{3.8}$$

$$\frac{\partial p}{\partial y} = -\frac{12\mu}{e^2}v_0 - \rho g, \tag{3.9}$$

$$\frac{\partial c}{\partial t} + \boldsymbol{u}_0 \cdot \nabla c = D\nabla^2 c. \tag{3.10}$$

It is well known, however, that solutions to these equations no longer satisy the corresponding three-dimensional Stokes equations.

Secondly, the simplified convection–diffusion equation (3.10) for the concentration field neglects several important effects contained in the full equation (2.3). It does not account for a cross-gap velocity component, and probably more importantly, it neglects the important effect of Taylor dispersion (Taylor 1953; Horne & Rodriguez 1983; Zimmerman & Homsy 1991; Petitjeans *et al.* 1999), i.e. the broadening of the front due to gradients in the velocity field. Given the above shortcomings of the Darcy equations, it is thus desirable to compare the stability results they give with those of the full three-dimensional Stokes equations.

By making the Darcy equations dimensionless with the same parameters (2.6)–(2.8) as the original Stokes equations, and then rewriting them in the streamfunction and vorticity formulation, we obtain

$$\nabla^2\psi = -\omega, \tag{3.11}$$

$$12\omega = -\frac{\partial c}{\partial x}, \tag{3.12}$$

$$\frac{\partial c}{\partial t} + \boldsymbol{u}_0 \cdot \nabla c = D\nabla^2 c. \tag{3.13}$$

Linearizing these equations, and assuming perturbations of the form

$$\psi'(x, y, t) = \hat{\psi}(y)\sin(\beta x)\,\mathrm{e}^{\sigma t}, \tag{3.14}$$

$$\omega'(x, y, t) = \hat{\omega}(y)\sin(\beta x)\,\mathrm{e}^{\sigma t}, \tag{3.15}$$

$$c'(x, y, t) = \hat{c}(y)\cos(\beta x)\,\mathrm{e}^{\sigma t}, \tag{3.16}$$

leads to the eigenvalue problem

$$\frac{\partial^2\hat{\psi}}{\partial y^2} - \beta^2\hat{\psi} = -\hat{\omega}, \tag{3.17}$$

$$12\hat{\omega} = \beta\hat{c}, \tag{3.18}$$

$$\sigma\hat{c} - \beta\frac{\partial c_0}{\partial y}\hat{\psi} = \frac{1}{Ra}\left(\frac{\partial^2\hat{c}}{\partial y^2} - \beta^2\hat{c}\right). \tag{3.19}$$

By once again incorporating a Reynolds-number-like term in the vorticity equation for better convergence properties, discretization by a Chebyshev approach leads to the matrix form of the eigenvalue problem as

$$\begin{pmatrix} \dfrac{\partial^2}{\partial y^2} - \boldsymbol{\beta}^2 & \boldsymbol{I} & \boldsymbol{0} \\ \boldsymbol{0} & 12\boldsymbol{I} & -\boldsymbol{\beta} \\ \boldsymbol{\beta}\bar{c} & \boldsymbol{0} & \dfrac{1}{Ra}\left(\dfrac{\partial^2}{\partial y^2} - \boldsymbol{\beta}^2\right) \end{pmatrix} \begin{pmatrix} \hat{\psi} \\ \hat{\omega} \\ \hat{c} \end{pmatrix} = \sigma \begin{pmatrix} \boldsymbol{0} & \boldsymbol{0} & \boldsymbol{0} \\ \boldsymbol{0} & Re\boldsymbol{I} & \boldsymbol{0} \\ \boldsymbol{0} & \boldsymbol{0} & \boldsymbol{I} \end{pmatrix} \begin{pmatrix} \hat{\psi} \\ \hat{\omega} \\ \hat{c} \end{pmatrix}. \tag{3.20}$$

This matrix problem can be solved with the ARPACK package, as described above. As far-field boundary conditions in the y-direction, we specify $\hat{\psi} = \hat{\omega} = \hat{c} = 0$.

3.3.2. *Comparison of stability results*

Figure 16 presents a comparison of the dispersion relationships obtained from the full three-dimensional Stokes equations and from Darcy's law for $\delta = 0.5$ and various Rayleigh numbers. Only for the smallest Ra value of 10^2 does there exist

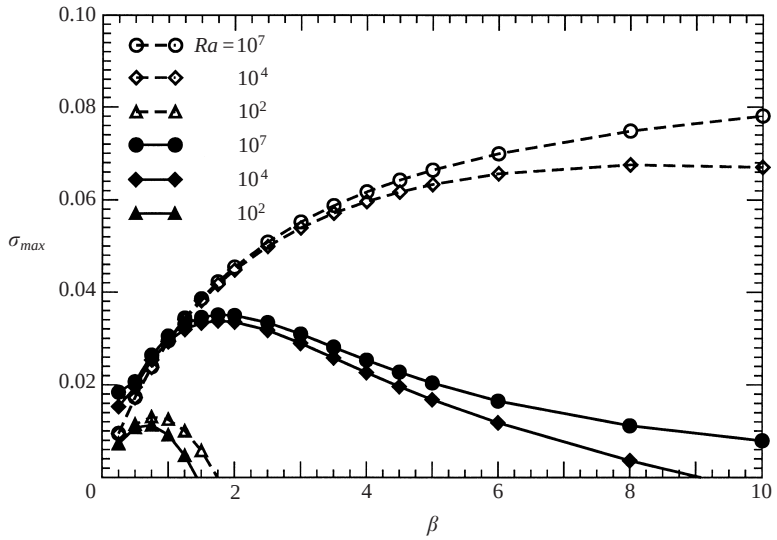

FIGURE 16. Dispersion relationships obtained from the three-dimensional Stokes equations (solid lines) and the extended Hele-Shaw equations (dashed lines) for $\delta = 0.5$ and various Rayleigh numbers. Only for the smallest *Ra* value do we observe at least qualitative agreement.

at least rough agreement between the two different sets of results. This is not unexpected, as for small Rayleigh numbers the diffusive spreading of the concentration front outweighs the convective Taylor dispersion, so that the concentration field is nearly independent of the cross-gap coordinate z. Under these conditions, the w-velocity component remains small, and the Hele-Shaw approach of employing a simplified, two-dimensional convection–diffusion equation for the concentration field is reasonably accurate.

For the *Ra* values of 10^4 and 10^7, there is not even qualitative agreement between the Hele-Shaw and the Stokes results. Naturally, Darcy's law cannot predict the predominantly two-dimensional 'gap mode' described earlier, which was observed in the experiments and nonlinear simulations by FKMP. Furthermore, in the limit of large *Ra*, the Stokes dispersion relationships show a pronounced maximum growth rate along with a high-wavenumber cutoff, whereas the Hele-Shaw growth rates keep increasing for large wavenumbers.

Figure 17 depicts the maximum growth rates obtained from the Stokes and Hele-Shaw equations, respectively, for various interface thickness parameters δ. The best agreement is observed for thick interfaces, where concentration variations in the cross-gap direction are small. For thinner interfaces, on the other hand, the Hele-Shaw growth rates are too large by more than a factor of two, and there is no clear indication of an asymptotic plateau.

For the extended Hele-Shaw approach, with increasing Rayleigh numbers maximum growth occurs at larger and larger wavenumbers, and the asymptotic plateau observed for the Stokes equation results in figure 13 is not reproduced. At $Ra = 10^7$, for example, the Hele-Shaw and Stokes results for the dominant wavelength at $\delta = 0.5$ differ by a factor of $O(50)$.

3.4. *Comparison with stability analysis based on the modified Brinkman equation*

For density-driven miscible flows in a vertical Hele-Shaw cell, FKPM present stability results based on a modified Brinkman equation, cf. also the more detailed account

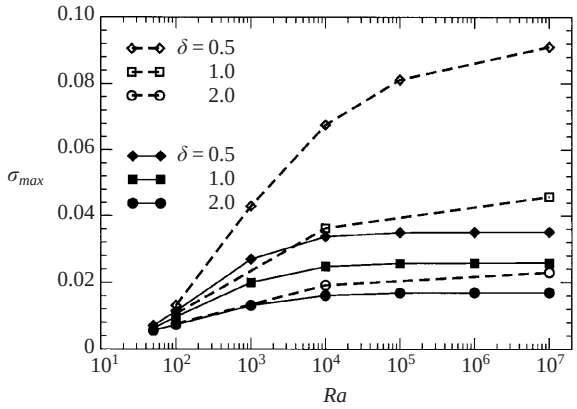

FIGURE 17. Maximum growth rate as a function of Ra for different δ. The solid lines are based on the Stokes equations, whereas the dashed lines represent results based on the extended Hele-Shaw approach.

provided by Fernandez *et al.* (2001). While this approach still involves a certain amount of averaging across the gap, it is not quite as restrictive as the extended Hele-Shaw equations described above. As a result, it was seen to provide a reasonably accurate prediction of growth rate and dominant wavenumber across the entire range of Rayleigh numbers. It is thus of interest to compare the predictions of the modified Brinkman approach with those of the full three-dimensional Stokes equations.

For a step profile of the concentration, and for the present definitions of the dimensionless growth rate and Rayleigh number, the modified Brinkman approach results in the implicit dispersion relationship

$$\sigma = \frac{12}{Ra} + \frac{\beta}{24}\left[1 - \frac{\beta}{\sqrt{12+\beta^2}}\right] - \frac{\beta}{2\sigma Ra}\left[1 - \frac{\beta}{\sqrt{\beta^2+\sigma Ra}}\right], \tag{3.21}$$

from which the growth rate can easily be determined as a function of β and Ra by means of a Newton iteration procedure. Figure 18 shows a comparison between the present Stokes results and those obtained from the Brinkman equation, for both the maximum growth rate and the corresponding wavenumber. While our present computational approach for the full three-dimensional Stokes equations cannot provide data for the step profile, extrapolating the data for different interface thickness parameters to $\delta = 0$ indicates that the modified Brinkman equation predicts the dominant wavenumbers quite accurately, whereas the predicted growth rates are probably somewhat too low. Nevertheless, there is no doubt that the Brinkman approach gives vastly superior results compared to the extended Hele-Shaw equations.

3.5. *Comparison with experimental measurements*

FKPM conducted density-driven experiments for fluids of constant viscosities in vertically arranged Hele-Shaw cells of different gap widths. They recorded both the wavelength of the dominant perturbation and its growth rate, as a function of the Rayleigh number. Consequently, we can perform direct comparisons of our stability results with their experimental observations. In order to do so, we have to multiply the growth rates obtained from the stability analysis by a factor of 12, and to divide Ra by the same factor. This is due to the slightly different definition of the characteristic quantities in the present stability analysis.

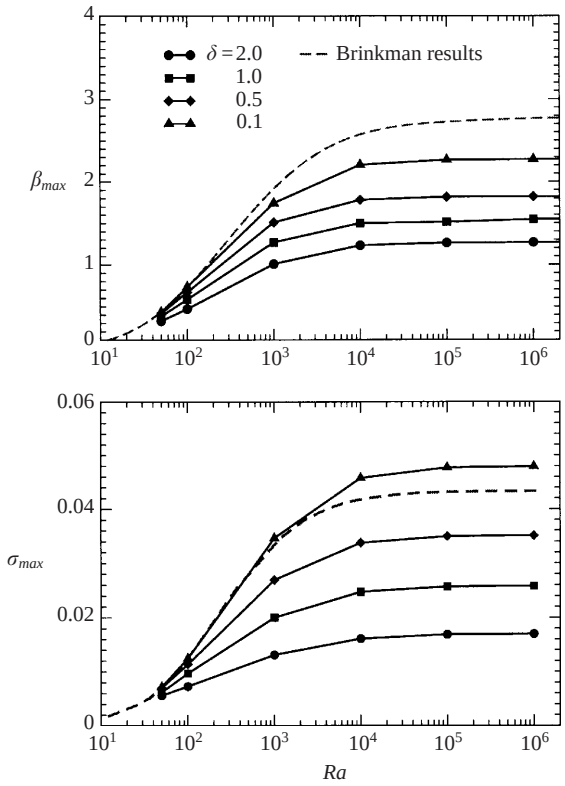

FIGURE 18. Comparison between the modified Brinkman and Stokes equation results for the maximum growth rate and the corresponding wavenumber.

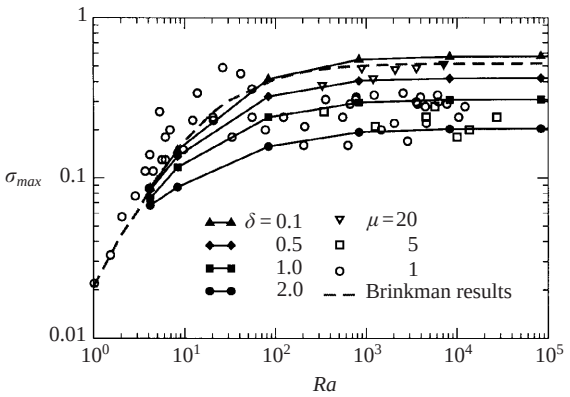

FIGURE 19. Experimental data of FKPM (open symbols) and stability results based on the Stokes (solid lines) and modified Brinkman (dashed line) equations for the maximum amplification rate as a function of the Rayleigh number.

Figure 19 displays growth rates as a function of *Ra*. The experimental data include fluids of different viscosities, while stability data are provided for various interface thickness parameters δ. For the sake of completeness, the modified Brinkman equation results for the step profile are included as well. Overall, the quantitative agreement between the experimental data and the stability results is quite good. A few interesting

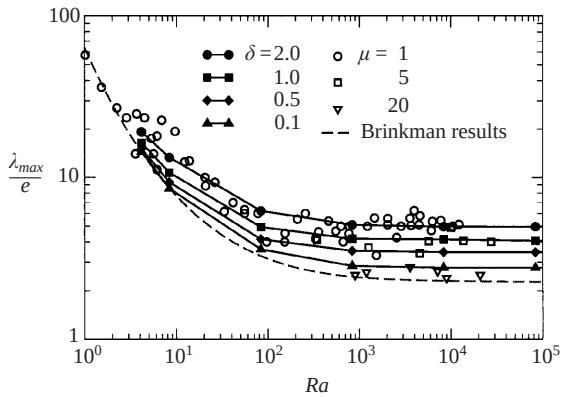

FIGURE 20. Experimental data of FKPM (open symbols) for the dominant wavelength as a function of the Rayleigh number. For comparison, stability results are provided based on the Stokes (solid lines) and modified Brinkman (dashed line) equations.

observations can be made. In general, the experimental data for the more viscous cases display higher growth rates than for the less viscous cases. From the Stokes–Einstein relation (e.g. Bird, Stewart & Lightfoot 1960) we know that the diffusion coefficient is approximately inversely proportional to the dynamic viscosity. The thickness of a diffused concentration layer originating from a step profile, in turn, is proportional to the square root of the diffusion coefficient and the elapsed time. If we assume that in the experiments the filling of the apparatus took roughly the same time independently of the fluid combination, the interface thickness should thus be proportional to the inverse of the square root of the viscosity. Consequently, the experimental data for $\mu = 1$ should correspond to a δ value that is $O(4–5)$ larger than the data for $\mu = 20$. While the considerable scatter in the experimental data prevent an accurate check, the data certainly show the correct tendency. There is a noticable overshoot of the low-viscosity experimental data for Rayleigh numbers of $O(10^1–10^2)$, which cannot be explained on the basis of the present stability analysis.

Figure 20 shows the corresponding experimental data and linear stability results for the wavelength of the dominant perturbation. Again the overall agreement is quite good. As for the growth rate, the experimental data for the more viscous fluids are seen to agree better with the stability results for thin interfaces, while the less viscous data correspond to thicker interfaces.

4. Conclusions

The above comparisons with experiments demonstrate that the discrepancy between experimental observations and stability results regarding the dominant wavelength in Hele-Shaw flows can be resolved by basing the linear theory on the three-dimensional Stokes equations, instead of Darcy's law. The agreement between the Stokes-based results and the experiments on one hand, and the disagreement between both of these and the Hele-Shaw results on the other hand, indicate the importance of the velocity component normal to the plane of the Hele-Shaw cell, and of concentration gradients across the gap. This is particularly true at high Rayleigh numbers. For low *Ra* values and large interfacial thickness parameters, the Hele-Shaw-based results are in better agreement, since the diffuse front prevents the development of significant three-dimensional effects.

For unstable density-driven flows in a vertical Hele-Shaw cell, the present linear stability analysis provides a clear resolution of the discrepancy between experimental observations and linear stability results derived on the basis of the gap-averaged Hele-Shaw approach. At the same time, the basic approach employed here of analysing a two-dimensional base state can be extended to address the stability of a variety of other, related flows. An analysis of viscously driven unstable flows will require the consideration of a main, net flow in the stability analysis, and the separate calculation of the two-dimensional base flow around which the linearization can subsequently be performed. The earlier simulations of Chen & Meiburg (1996) will be useful in this regard. Further possible extensions could address the effects of finite Reynolds numbers, temperature effects or chemical reactions at the front. Efforts in this direction are currently underway.

This work was begun while E. M. was a visitor at the Institute of Fluid Dynamics at ETH Zürich. The hospitality of the members of the IFD, especially Professor Leonhard Kleiser, is gratefully acknowledged. We furthermore appreciate the close collaboration with Drs Petitjeans, Kurowski and Fernandez of LPMMH at ESPCI, Paris, as well as helpful discussions with Dr Dirk Wilhelm. Additional support was received from the NSF/ITR and NASA Microgravity programs, from DOE, the donors of The Petroleum Research Fund (grant ACS-PRF# 33497-AC9), and from Chevron Petroleum Technology Company.

REFERENCES

Batchelor, G. K. & Nitsche, J. M. 1991 Instability of stationary unbounded stratified fluid. *J. Fluid Mech.* **227**, 357.

Batchelor, G. K. & Nitsche, J. M. 1993 Instability of stratified fluid in a vertical cylinder. *J. Fluid Mech.* **252**, 419.

Bird, R. B., Stewart, W. E. & Lightfoot, E. N. 1960 *Transport Phenomena*. John Wiley & Sons.

Bretherton, F. B. 1961 The motion of long bubbles in tubes. *J. Fluid Mech.* **10**, 166.

Brinkman, H. C. 1947 A calculation of the viscous force exerted by a flowing fluid on a dense swarm of particles. *Appl. Sci. Res.* **A1**, 27.

Chandrasekhar, S. 1961 *Hydrodynamic and Hydromagnetic Stability*. Oxford University Press.

Chen, C.-Y. & Meiburg, E. 1996 Miscible displacements in capillary tubes. Part 2. Numerical simulations. *J. Fluid Mech.* **326**, 57.

Chen, C.-Y. & Meiburg, E. 1998 Miscible porous media displacements in the quarter five-spot configuration. Part 1. The homogeneous case. *J. Fluid Mech.* **371**, 233.

Chuoke, R. L., Van Meurs, P. & Van der Poel, C. 1959 The instability of slow, immiscible, viscous liquid–liquid displacements in permeable media. *Trans. Am. Inst. Min. Metall. Pet. Engng* **216**, 188.

Fernandez, J., Kurowski, P., Limat, L., & Petitjeans, P. 2001 Rayleigh-Taylor instability inside Hele-Shaw cells: A new approach of wavelength selection problem. *Phys. Fluids* (in press).

Fernandez, J., Kurowski, P., Petitjeans, P. & Meiburg, E. 2002 Density-driven, unstable flows of miscible fluids in a Hele-Shaw cell. *J. Fluid Mech.* **451**, 239 (referred to herein as FKPM)

Homsy, G. M. 1987 Viscous fingering in porous media. *Annu. Rev. Fluid Mech.* **19**, 271.

Horne, R. N. & Rodriguez, F. 1983 Dispersion in tracer flow in fractured geothermal systems. *Geophys. Res. Lett.* **10**, 289.

Lajeunesse, E., Martin, J., Rakotomalala, N. & Salin, D. 1997 3D instablity of miscible displacements in a Hele-Shaw cell. *Phys. Rev. Lett.* **79**, 5254.

Lajeunesse, E., Martin, J., Rakotomalala, N., Salin, D. & Yortsos, Y. C. 1999 Miscible displacements in a Hele-Shaw cell at high rates. *J. Fluid Mech.* **398**, 299.

Lehoucq, R. B., Sorensen, D. C. & Yang, C. 1998 *ARPACK USERS GUIDE: Solution of Large Scale Eigenvalue Problems with Implicitly Restarted Arnoldi Methods*. SIAM, Philadelphia.

Lele, S. K. 1992 Compact finite difference schemes with spectral-like resolution. *J. Comput. Phys.* **103**, 16.

Manickam, O. & Homsy, G. M. 1993 Stability of miscible displacements in porous media with nonmonotonic viscocity profiles. *Phys. Fluids* A **5**, 1356.

Manickam, O. & Homsy, G. M. 1995 Fingering instabilities in vertical miscible displacement flows in porous media. *J. Fluid Mech.* **288**, 75.

Martin, J., Rakotomalala, N. & Salin, D. 2001 Gravitational instability of miscible fluids in a Hele-Shaw cell. Preprint.

Maschhoff, M. J. & Sorensen, D. C. 1996 P-ARPACK: An efficient portable large scale eigenvalue package for distributed memory parallel architectures. *Applied Parallel Computing in Industrial Problems and Optimization*. Lecture Notes in Computer Science, vol. 1184. Springer, Berlin.

Maxworthy, T. 1989 Experimental study of interface instability in a Hele-shaw cell. *Phys. Rev.* A **39**, 5863.

Park, C. W., Gorell, S. & Homsy, G. M. 1984 Two-phase displacement in Hele-Shaw cells: experiments on viscously driven instabilities. *J. Fluid Mech.* **141**, 275.

Park, C.-W. & Homsy, G. M. 1984 Two-phase displacements in Hele-Shaw cells: Theory. *J. Fluid Mech.* **139**, 291.

Park, C.-W. & Homsy, G. M. 1985 The instability of long fingers in Hele-Shaw flows. *Phys. Fluids* **28**, 1583.

Paterson, L. 1985 Fingering with miscible fluids in a Hele-shaw cell. *Phys. Fluids* **28**, 26.

Petitjeans, P., Chen, C.-Y., Meiburg, E. & Maxworthy, T. 1999 Miscible quarter five-spot displacements in a Hele-Shaw cell and the role of flow-induced dispersion. *Phys. Fluids* **7**, 1705.

Petitjeans, P. & Maxworthy, T. 1996 Miscible displacements in capillary tubes. Part 1. Experiments. *J. Fluid Mech.* **326**, 37.

Rogerson, A. & Meiburg, E. 1993*a* A Shear stabilization of miscible displacement process in porous media. *Phys. Fluids* A **5**, 1344.

Rogerson, A. & Meiburg, E. 1993*b* Numerical simulation of miscible displacement processes in porous media flows under gravity. *Phys. Fluids* A **5**, 2644.

Ruith, M. & Meiburg, E. 2000 Miscible rectilinear displacements with gravity override. Part 1. Homogeneous porous medium. *J. Fluid Mech.* **420**, 225.

Saffman, P. G. & Taylor, G. I. 1958 The penetration of a fluid into a porous medium or Hele-Shaw cell containing a more viscous liquid *Proc. R. Soc. Lond.* A **245**, 312.

Schwartz, L. 1986 Stability of Hele-Shaw flows: The wetting-layer effect. *Phys. Fluids* **29**, 3086.

Sorensen, D. C. 1992 Implicit application of polynomial filters in a k-step Arnoldi method. *SIAM J. Matrix Anal. Appl.* **13**, 357.

Tan, C. T. & Homsy, G. M. 1986 Stability of miscible displaccements in porous media: Rectilinear flow. *Phys. Fluids* **29**, 3549.

Tan, C. T. & Homsy, G. M. 1988 Simulation of nonlinear fingering in miscible displacement. *Phys. Fluids* **31**, 1330.

Taylor, G. I. 1950 The instability of liquid surfaces when accelerated in a direction perpendicular to their planes. *Proc. R. Soc. Lond.* A **201**, 192.

Taylor, G. I. 1953 Dispersion of soluble matter in solvent flowing slowly through a tube. *Proc. R. Soc. Lond.* A **219**, 186.

Wooding, R. A. 1960 Instability of a viscous liquid of variable density in a vertical Hele-Shaw cell. *J. Fluid Mech.* **7**, 501.

Wooding, R. A. 1969 Growth of fingers at an unstable diffusing interface in a porous medium or Hele-Shaw cell. *J. Fluid Mech.* **39**, 477.

Wooding, R. A., Tyler, S. W. & White, I. 1997 Convection of groundwater below an evaporating salt lake: 1. Onset of instability. *Water Resour. Res.* **33**, 1199.

Yortsos, Y. C. 1990 Instabilities in displacement processes in porous media. *J. Phys. Condens. Matter* **2**, SA443.

Zimmerman, W. B. & Homsy, G. M. 1991 Viscous fingering in miscible displacement with anisotropic dispersion. *Phys. Fluids* A **3**, 1859.